

# Observations of the *Hubble Deep Field South* with the *Infrared Space Observatory* – I. Observations, data reduction and mid-infrared source counts

Seb Oliver,<sup>1,2</sup> Robert G. Mann,<sup>1,3★</sup> Ruth Carballo,<sup>4,5</sup> Alberto Franceschini,<sup>6</sup> Michael Rowan-Robinson,<sup>1</sup> Maria Kontizas,<sup>7</sup> Anastasios Dapergolas,<sup>8</sup> Evangelhos Kontizas,<sup>8</sup> Aprajita Verma,<sup>1</sup> David Elbaz,<sup>9</sup> Gian Luigi Granato,<sup>6</sup> Laura Silva,<sup>10</sup> Dimitra Rigopoulou,<sup>11</sup> J. Ignacio Gonzalez-Serrano,<sup>5</sup> Steve Serjeant,<sup>1,12</sup> Andreas Efstathiou<sup>1</sup> and Paul P. van der Werf<sup>13</sup>

<sup>1</sup>*Astrophysics Group, Imperial College London, Blackett Laboratory, Prince Consort Road, London SW7 2BZ*

<sup>2</sup>*Astronomy Centre, School of Chemistry, Physics and Environmental Science, University of Sussex, Falmer, Brighton BN1 9QJ*

<sup>3</sup>*Institute for Astronomy, University of Edinburgh, Royal Observatory, Blackford Hill, Edinburgh EH9 3HJ*

<sup>4</sup>*Departamento de Matematica Aplicada y CC, Universidad de Cantabria, Avda. Los Castros s/n, 39005 Santander, Spain*

<sup>5</sup>*Instituto de Física de Cantabria (CSIC-UC), Avda. Los Castros s/n, 39005 Santander, Spain*

<sup>6</sup>*Dipartimento di Astronomia, Università di Padova, Vicolo dell'Osseatorio 5, I-35122, Padova, Italy*

<sup>7</sup>*Department of Physics, University of Athens, Panepistimiopolis, GR-15783, Zografos, Greece*

<sup>8</sup>*Astronomical Institute, National Observatory of Athens, Lofos Nymfon, Thission, PO Box 20048, 11810 Athens, Greece*

<sup>9</sup>*DSM/DAPNIA/SAP, CE-Saclay, Orme des Merisiers – Bat 709, 91191 Gif-sur-Yvette Cedex, France*

<sup>10</sup>*Astrophysics Sector, SISSA, Via Beirut 2-4, 34013 Trieste, Italy*

<sup>11</sup>*Max-Planck-Institut für extraterrestrische Physik, Postfach 1603, 85740 Garching, Germany*

<sup>12</sup>*Unit for Space Sciences and Astrophysics, School of Physical Sciences, University of Kent, Canterbury CT2 7NZ*

<sup>13</sup>*Leiden Observatory, PO Box 9513, NL-2300 RA Leiden, the Netherlands*

Accepted 2001 December 19. Received 2001 December 19; in original form 2001 June 19

## ABSTRACT

We present results from a deep mid-infrared survey of the *Hubble Deep Field South* (HDF-S) region performed at 6.7 and 15  $\mu\text{m}$  with the ISOCAM instrument on board the *Infrared Space Observatory* (ISO). The final map in each band was constructed by the co-addition of four independent rasters, registered using bright sources securely detected in all rasters, with the absolute astrometry being defined by a radio source detected at both 6.7 and 15  $\mu\text{m}$ . We sought detections of bright sources in a circular region of radius 2.5 arcmin at the centre of each map, in a manner that simulations indicated would produce highly reliable and complete source catalogues using simple selection criteria. Merging source lists in the two bands yielded a catalogue of 35 distinct sources, which we calibrated photometrically using photospheric models of late-type stars detected in our data. We present extragalactic source count results in both bands, and discuss the constraints that they impose on models of galaxy evolution, given the volume of space sampled by this galaxy population.

**Key words:** surveys – galaxies: evolution – galaxies: formation – galaxies: Seyfert – galaxies: starburst – infrared: galaxies.

## 1 INTRODUCTION

One of the most notable achievements of the *Hubble Space Telescope* (HST) has been to lead and inspire the concerted multiwavelength programme of observations of the *Hubble Deep Field* (HDF; Williams et al. 1996) region. As part of that campaign

we observed the HDF at 6.7 and 15  $\mu\text{m}$  using the ISOCAM instrument (Cesarsky et al. 1996) on the *Infrared Space Observatory* (ISO; Kessler et al. 1996). From the maps that resulted from these observations (Serjeant et al. 1997) we extracted sources in both bands (Goldschmidt et al. 1997), the number counts of which implied a strongly evolving population of starburst galaxies (Oliver et al. 1997). Following the association of these sources with galaxies in optical HDF catalogues (Mann et al. 1997) we derived

★E-mail: rgm@roe.ac.uk

**Table 1.** *ISO* observation log. This table gives some details from the *ISO* data bases for each of the *ISO* HDF-S observations: the target name, coordinates, observation number (OSN), time spent on target in seconds (TDT), revolution number (REV), status and date. Note that two observations (OSN 4 and 8) failed, but were repeated on November 27 and 29.

TARGET	RA (J2000) h m s	Dec. (J2000) ° ′ ″	OSN	TDT	REV	STATUS	Date
HDF-1 LW2	22 32 57.5	−60 33 10.0	1	7825	702	Observed	1997 Oct 17
HDF-4 LW2	22 32 53.9	−60 33 00.0	7	7825	702	Observed	1997 Oct 17
HDF-2 LW2	22 32 56.4	−60 32 51.8	3	7825	704	Observed	1997 Oct 17
HDF-4 LW3	22 32 53.9	−60 33 00.0	8	7497	722	Failed	1997 Nov 6
HDF-2 LW3	22 32 56.4	−60 32 51.8	4	7497	722	Failed	1997 Nov 6
HDF-3 LW2	22 32 55.0	−60 33 18.2	5	7825	723	Observed	1997 Nov 7
HDF-3 LW3	22 32 55.0	−60 33 18.2	6	7497	723	Observed	1997 Nov 7
HDF-1 LW3	22 32 57.5	−60 33 10.0	2	7497	723	Observed	1997 Nov 8
HDF-4 LW3	22 32 53.9	−60 33 00.0	8	7497	742	Observed	1997 Nov 27
HDF-2 LW3	22 32 56.4	−60 32 51.8	4	7497	745	Observed	1997 Nov 29

**Table 2.** Observation parameters for the *ISO* HDF-S.

Parameter	OSN	
	1,3,5,7	2,4,6,8
Filter	LW2	LW3
Band centre ( $\mu\text{m}$ )	6.7	15
Gain	2	2
Tint (s)	10	5
NEXP	10	20
NSTAB	80	80
PFOV (arcsec)	6	6
M,N	8,8	8,8
dM, dN (arcsec)	27	27

an infrared luminosity density that suggested a higher star formation rate in the HDF region than indicated by optical studies (Rowan-Robinson et al. 1997); the importance of dust obscuration in estimating the star formation rate has been confirmed by other *ISO* surveys (e.g. Flores et al. 1999), from detailed consideration of the optical measures of star formation (Steidel et al. 1999) and from the intercomparison of different star formation indices (Cram et al. 1998).

Difficulties with the *ISO* 6.7- $\mu\text{m}$  data led us to re-observe the HDF at that wavelength. These new data, together with a consensus view of the interpretation of our *ISO Hubble Deep Field North* (HDF-N) data derived from the combined experience of the several groups that re-analysed them (Aussel et al. 1999; Desert et al. 1999) in the light of developing knowledge of the properties of ISOCAM data, will be the topic of a subsequent paper, as will a revised and updated scientific interpretation of the *ISO* HDF data.

Following the success of the HDF project, a similar programme of *HST* observations was planned for the southern hemisphere, and the region of the *Hubble Deep Field South* (HDF-S) has become the target of a similarly wide-ranging multiwavelength programme<sup>1</sup> of observations. This paper describes our contribution to that project, through our mapping of the HDF-S with ISOCAM. We mapped the HDF-S Wide Field Planetary Camera 2 (WFPC2) fields at both 6.7 and 15  $\mu\text{m}$ , as in the northern HDF, but with a slightly different observational strategy (described in Section 2), motivated by our experience with the *ISO* HDF data. Section 3 describes our data reduction procedures, and Sections 4 and 5

describe source extraction and photometric calibration, respectively. In Section 6 we describe simulations of the data performed to facilitate assessment of the reliability of the source catalogues that we present in Section 7, and to compute the effective area of the survey as a function of flux cut, as this is required for computation of the source counts, which is the topic of Section 8. Finally, Section 9 presents a discussion of the results of this paper and the conclusions that we draw from them. In an accompanying paper (Mann et al. 2002, hereafter Paper II) we seek associations for these sources in optical/near-infrared and radio surveys of the HDF-S region, and present star formation rate estimates for the sources for which we find associations.

## 2 THE OBSERVATIONS

The team undertaking the European Large Area *ISO* Survey (ELAIS;<sup>2</sup> Oliver et al. 2000) were awarded 61.3 ks to observe the HDF-S in a successful application to the *ISO* Supplemental Call. The observations were carried out using the ISOCAM instrument (Cesarsky et al. 1996) between 1997 October 17 and November 29. In the light of an increased understanding of the properties of ISOCAM data, and of the galaxy population that they probe, gained by our own *ISO* HDF observations and from other deep ISOCAM surveys (e.g. Taniguchi et al. 1997; Elbaz et al. 1999), we made some alterations to the observing strategy that we used for the *ISO* HDF, as reported by Serjeant et al. (1997).

As listed in Table 1, eight rasters were taken, one with the LW2 (6.7  $\mu\text{m}$ ) and one with the LW3 (15  $\mu\text{m}$ ) filter at each of four positions, with raster centres offset by fractional pixel widths to improve the spatial resolution of the final map obtained by their co-addition. The parameters used for these observations are listed in Table 2. The values for *Gain*, *Tint* (the integration time per readout), *NEXP* (the number of readouts per pointing) and *NSTAB* (the number of readouts allowed for stabilization prior to the raster) remained unchanged, as those used by Serjeant et al. (1997) still appeared to be optimal for the required depth. The pixel field of view, *PFOV*, at 6.7  $\mu\text{m}$  was changed from 3 to 6 arcsec (matching that used at 15  $\mu\text{m}$ ), since the *ISO* HDF images at 6.7  $\mu\text{m}$  were not confusion limited, and the improvement in signal-to-noise ratio and areal coverage obtained by moving to larger pixels was expected to outweigh the loss in resolution. The other significant change was to increase the raster step size, which had two effects. First, with the step size now larger than the point spread function

<sup>1</sup>Details of the HDF-S programme can be found at <http://www.stsci.edu/ftp/science/hdf/hdfsouth/hdfs.html>

<sup>2</sup>For details see the ELAIS home page: <http://astro.ic.ac.uk/elais>

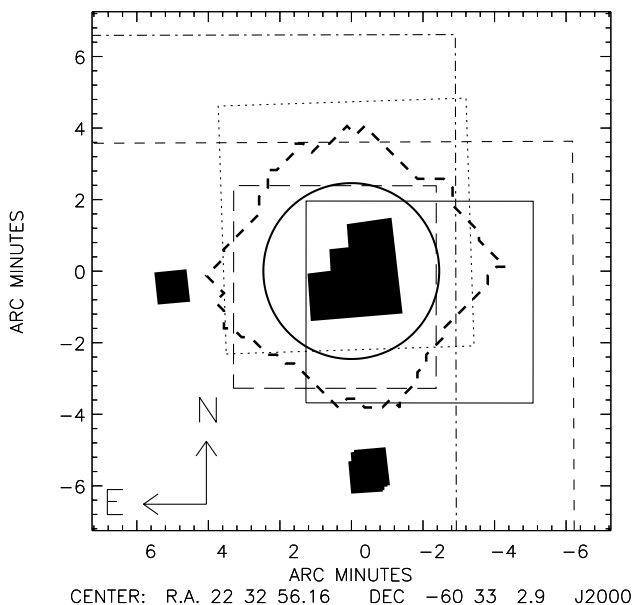


**Figure 1.** The location of our *ISO* rasters with respect to those of other data sets taken in the area. The shaded regions mark the *HST* fields, with the STIS and NICMOS fields to the east and south of the WFPC2 field, respectively. The thick-dashed irregular shape and the solid circle show, respectively, the maximum extent of our *ISO* coverage (the coverage in the two bands differs slightly) and the region from which the source catalogues of Section 7 were selected. The remaining lines show boundaries of four optical/near-infrared surveys discussed in Paper II, as follows: (i) dotted line – AAT prime focus imaging survey of Verma et al. (in preparation); (ii) dashed line – CTIO Big Throughput Camera (BTC) survey of Gardner et al. (1999); (iii) dot-dashed line – CTIO BTC survey of Walker (1999); (iv) solid line – ESO Imaging Survey (EIS) optical imaging survey of da Costa et al. (1998); and (v) long-dashed line – ESO EIS near-infrared survey of da Costa et al. (1998).

(PSF), consecutive pointings would no longer have significantly correlated signal, making the removal of noise that was correlated in time (e.g.  $1/f$  noise) much easier. Secondly, the larger pixel area meant that the full survey area could be covered by each individual  $8 \times 8$  raster, with the complete survey being made up by stacking the four independent rasters in each passband. This contrasts with the technique adopted in the *ISO* HDF of partially overlapping deeper rasters, and has several advantages: it reduces correlated noise problems; readily provides direct assessment of source reliability, through looking for detections in the independent maps; and facilitates the registration of the maps, through the presence of a greater number of bright sources in each raster (helped further by the lower Galactic latitude of the HDF-S, providing more bright stellar sources). In Fig. 1 we show the location of our *ISO* rasters with respect to those of various optical/near-infrared data sets taken in the HDF-S area: this illustrates that, while none of these surveys covers the whole of the area that we mapped with *ISO*, the region from which we select sources in Section 7 is covered, at least partially, by several imaging surveys in different wavebands, as discussed in more detail in Paper II.

### 3 DATA REDUCTION

Similarly to the *ISO* HDF data, and in contrast to the ELAIS data (Oliver et al. 2000), we do not expect to detect many sources in the signal from a single pixel as it scans across the sky (the ‘time-line’). Most sources will only be detected when all the overlapping

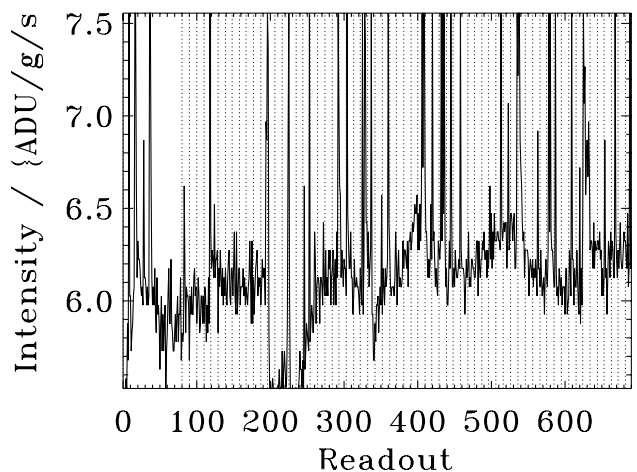


**Figure 2.** Example pixel history. Minimum and maximum levels are adjusted to exclude extreme outliers. The positions of slews are marked with vertical dotted lines. This particular pixel is row 16, column 16 from the  $6.7\text{-}\mu\text{m}$  observation HDF-1.

scans are co-added. The data reduction thus proceeds by filtering each time-line for artefacts and then combining these to produce a map for each raster. These raster maps are then co-aligned and co-added to produce a single map from which sources can be extracted. Most of the data reduction described in these sections was carried out using the Interactive Data Language IDL,<sup>3</sup> with some steps done using the ISOCAM Interactive Analysis (CIA: Ott et al. 1998) software.

#### 3.1 Time-series filtering

The first stage in the data reduction treats the scan of each pixel across the sky independently. This time series is filtered to reduce the impact of noise features and optimize the signal at each static pointing. At this stage the individual pixel responses are also estimated using a Gaussian fit to the scan to determine a sky flat-field correction which is normalized to the median from the central pixels, as in Serjeant et al. (1997).

The original data reduction of the *ISO* HDF applied a simple threshold filtering of very short-time-scale features (cosmic ray hits), and we apply the same method to these data. However, for the original reduction of the *ISO* HDF data we anticipated that there might be significant source confusion, leading to real structure in the sky background, and so we did not apply any filtering for low-frequency noise. At  $6.7\text{ }\mu\text{m}$  the *ISO* HDF was not significantly confused and the revised observing strategy that we used for the HDF-S reduces any correlated signal between successive pointings. We thus decided to adopt a more aggressive filtering strategy for these data. It can be seen from Fig. 2 that there is significant correlated noise at a variety of time-scales. The filtering technique we adopt is similar to that used by Desert et al. (1999). We subtract a time-variable background level from all the readouts in a time-line. The background level is estimated for each pointing, being the average of the readouts in the two previous and the two subsequent pointings.

This filtering scheme will go awry where sources lie in the pixels used for background estimation, so we perform a second iteration. We mask out the bright sources detected from the first pass (see Section 4) and then an additional filter is applied to exclude readouts not already flagged as sources that deviate from the

<sup>3</sup>See [www.rsinc.com](http://www.rsinc.com)

**Table 3.** Statistical properties of the reduced data sets. All units are instrumental ( $\text{ADU gain}^{-1} \text{s}^{-1} \text{pixel}^{-1}$ ). The mode is taken from all valid readouts and pixels. Fluctuations are estimated by fitting a Gaussian to the distribution (first lines) and by calculating the rms (second lines). The difference between these two measures gives some idea of the non-Gaussianity. Fluctuations are quoted for the readout and pointing time-scales (third and fourth columns) and are estimated from the time-line of one pixel near the centre of the image. In the filtered readouts the rms fluctuations are similar to the  $\sigma$  estimated from a Gaussian fitting, suggesting that the noise is reasonably Gaussian. If the fluctuations are white noise they should reduce by a factor of  $\sqrt{NEXP}$  (i.e.  $\sqrt{10}$  at  $6.7 \mu\text{m}$  and  $\sqrt{20}$  at  $15 \mu\text{m}$ ) when averaging over a pointing. The fluctuations over an entire detector image (after co-addition of all readouts in a pointing) are quoted in column 5 and estimated from all valid pixels and images. The noise in the images is calculated separately for regions with different numbers of pointings and is fitted as  $\sqrt{NPOINT}$ ; the values quoted in the table are for  $NPOINT = 1$ , and for our maps  $NPOINT \sim 13$ . Finally, we compute the noise statistics for one of our mis-mosaicked maps (as described in Section 6); column 6. Here we only quote the  $\sigma$  values as the rms measures are more strongly influenced by the residual source signals in parts of the images with small values of  $NPOINT$ .

Observation	Mode	Readout		Point.	Image	Mis-mosaicked
		Raw	Filt.			
HDF-1 LW2	6.30	0.21	0.14	0.08	0.089	0.088
		2.98	0.14			
HDF-2 LW2	6.47	0.13	0.11	0.06	0.081	0.079
		1.90	0.11			
HDF-3 LW2	7.38	0.43	0.19	0.19	0.11	0.10
		3.88	0.21			
HDF-4 LW2	6.37	0.20	0.13	0.08	0.083	0.083
		2.32	0.14			
HDF-1 LW3	33.49	0.33	0.13	0.13	0.22	0.25
		0.32	0.06			
HDF-2 LW3	37.39	0.30	0.12	0.12	0.24	0.26
		0.29	0.05			
HDF-3 LW3	34.04	0.34	0.18	0.18	0.23	0.25
		0.34	0.14			
HDF-4 LW3	35.09	1.53	1.50	1.50	1.28	1.28
		1.23	2.80			

estimated background by more than  $5\sigma$ . This procedure will not affect remaining sources which would be at a very low level of significance in single pointings. After applying these filters the mean of the readouts is calculated over each pointing, and the resulting noise statistics are summarized in Table 3.

### 3.2 Mosaicking independent rasters

The detector image at each raster position needs to be projected on to the sky. For this process we use a ‘shift-and-add’ technique. We generate a blank sky map with 1-arcsec pixels. Then for each raster pointing we determine which sky pixels lie within the geometrical footprint of each detector pixel. In doing this we take into account the field distortions (Aussel et al. 1999) in the ISOCAM data: Note that it was not possible to take these into account in our original ISO HDF-N reductions since the distortions had not been well characterized at that time. The average intensity of all detectors covering a sky pixel is calculated using a number of estimators. It was found that the median produced the smallest fluctuations in the resulting sky maps (suggesting that some residual non-Gaussian noise was present), and so we adopt this estimator. The use of the geometrical footprint was a somewhat arbitrary choice and not the optimal one for point sources; since in the extraction of point sources we convolve the image with another kernel, we have broadened the effective PSF by using this.

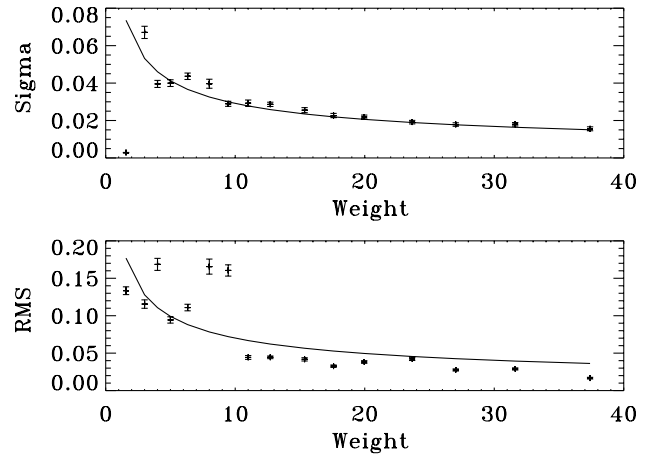


**Figure 3.** Noise estimates as a function of number of pointings ( $NPOINT$ , labelled as ‘Weight’), for the LW2 ( $6.7 \mu\text{m}$ ) HDF-1 observations. Upper panel:  $\sigma$  from a Gaussian fit; lower panel: rms. All units are  $\text{ADU gain}^{-1} \text{s}^{-1} \text{pixel}^{-1}$ .

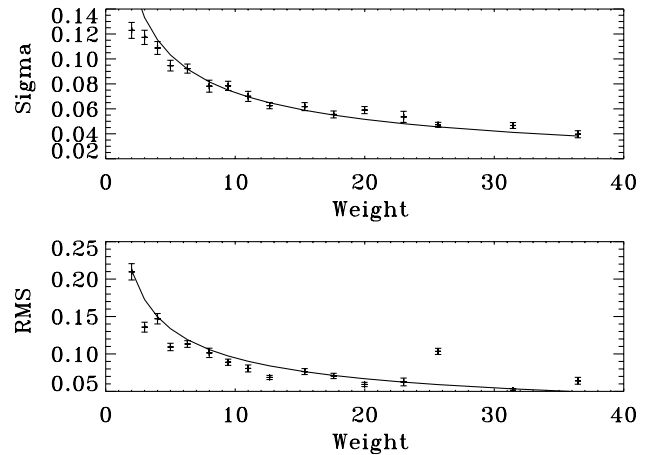


**Figure 4.** As Fig. 3, for the LW3 ( $15 \mu\text{m}$ ) HDF-1 observations.

The noise in these maps is estimated by constructing a histogram of pixel values and fitting this with a Gaussian, as well as computing an rms directly. However, since the number of independent pointings varies as a function of sky position, we calculate these statistics for regions with similar numbers of pointings. The results from these assessments indicate that noise reduces as expected for independent pointings (i.e. the residual noise correlations between pixels are at a very low level: see Figs 3 and 4). The rms fluctuations in the maps are larger than the  $\sigma$  estimated from the Gaussian fitting, indicating non-Gaussian fluctuations, which we attribute to real sources, either distinct or confused.

The noise can also be investigated by corrupting the astrometry information and thereby diluting the signal from real sources. We describe this ‘mis-mosaicking’ technique in more detail in Section 6. The noise statistics from a typical mis-mosaicked field, together with those from the final images, are also summarized in Table 3. The  $\sigma$  values from the mis-mosaicked fields are very similar to the real fields, confirming that these are reasonably representative of the noise. The rms values for the mis-mosaicked fields were invariably higher, but this was because the rms values in regions of lower coverage were higher, since real sources could not be properly filtered out in these regions: this is consistent with our hypothesis that much of any residual non-Gaussian noise is due to real sources.

### 3.3 Raster registration

Since the survey strategy means that each independent raster covers approximately the same relatively large area (cf. *ISO* HDF), a number of bright sources are clearly visible in each raster. For each band we thus select a number of these sources that had good signal-to-noise ratio and which were not located close to the edges of the map (where the noise is less well behaved and the field distortions are more significant) for use in registering the four maps. The positions of these sources are denoted by  $(x_{i,j}, y_{i,j})$ , where the  $i$  subscript labels the source and the  $j$  subscript labels the map. We then compute the mean  $(\bar{x}_i, \bar{y}_i)$  position of each source across all four independent maps, weighted by  $w_j$ , the mean signal-to-noise ratio of that map (estimated from the mean signal-to-noise ratio in all the sources). For each map we then estimate a mean offset  $\delta x_j = \sum w_i(x - \bar{x}_i) / \sum w_i$ , where the weight for each source  $w_i$  is estimated from the mean signal-to-noise ratio for that source over all maps. This process does not require any assumptions about the relationship between the *ISO* sources and sources detected in any other wavebands, and is also likely to be more robust than the cross-correlation of the full image (including the noisy regions) with, for example, a radio map of the same field. The mean offsets are rounded to the nearest pixel (1 arcsec). The overall astrometric reference frame is defined later: see Section 7 below.

The registered images are then co-added using an inverse variance weighting. The variance estimated is proportional to the

number of pointings within a raster and scaled using the value for  $\sigma/\sqrt{NPOINT}$  estimated from the Gaussian fitting described above. The resulting maps have some small residual background. This background (which is not always positive) should in principle have been removed by the time-line filtering, although some residual would be expected from an overall gradient in the time-lines. In any case, the background is estimated from the mean of the Gaussian fitted to the histogram of the map pixel values, which is a good estimate of the mode. The resulting co-added signal-to-noise ratio maps at 6.7 and 15  $\mu\text{m}$  are presented in Figs 5 and 6, respectively.

## 4 SOURCE DETECTION

We expect most of the sources in these maps to be point sources, so it is more appropriate to detect sources by a convolution technique rather than to use a connected pixel algorithm. We also expect to be close to the confusion limit, so the choice of smoothing kernel is important: where the signal is dominated by a single source the optimal kernel is the PSF, while for confused images the likely presence of other sources in the wings of the PSF will make this kernel non-optimal. The solution is either to truncate the PSF kernel at some appropriate distance or to use a narrower kernel. Theoretically, the PSF should be that of the Airy disc defined by the telescope aperture, convolved with the square pixel aperture of 6 arcsec, and the CIA calibration PSFs are similar to this. In

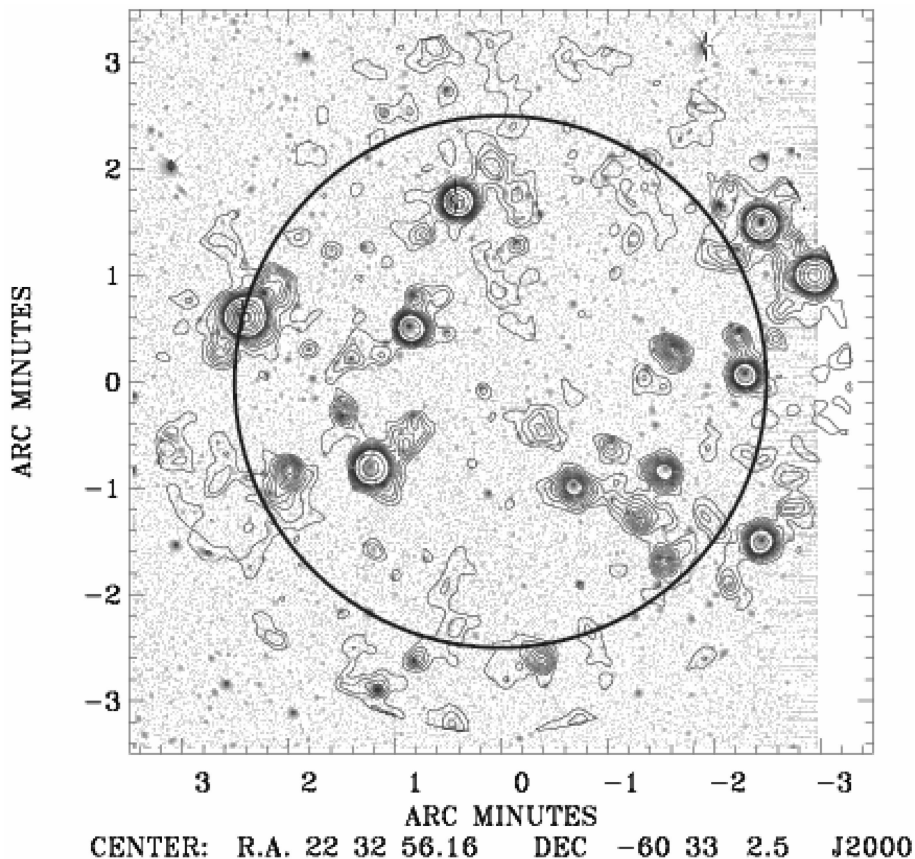


**Figure 5.** LW2 (6.7  $\mu\text{m}$ ) signal-to-noise ratio map. This Fig. plots contours in the LW2 signal-to-noise ratio map after it has been smoothed with the point-source-detection kernel. The lowest contour level has signal-to-noise ratio = 1 and subsequent intervals are 1 until signal-to-noise ratio = 10 after which the contours are logarithmically spaced. *ISO* data are plotted out to a radius of 3.3 arcmin. The background image is the CTIO BTC survey of Walker (1999). The circle indicates the 2.5-arcmin boundary of the region within which we extracted sources for our catalogues. Overlays of subsections of the data on to colour *HST* images are available from our WWW page (<http://astro.ic.ac.uk/hdfs>).

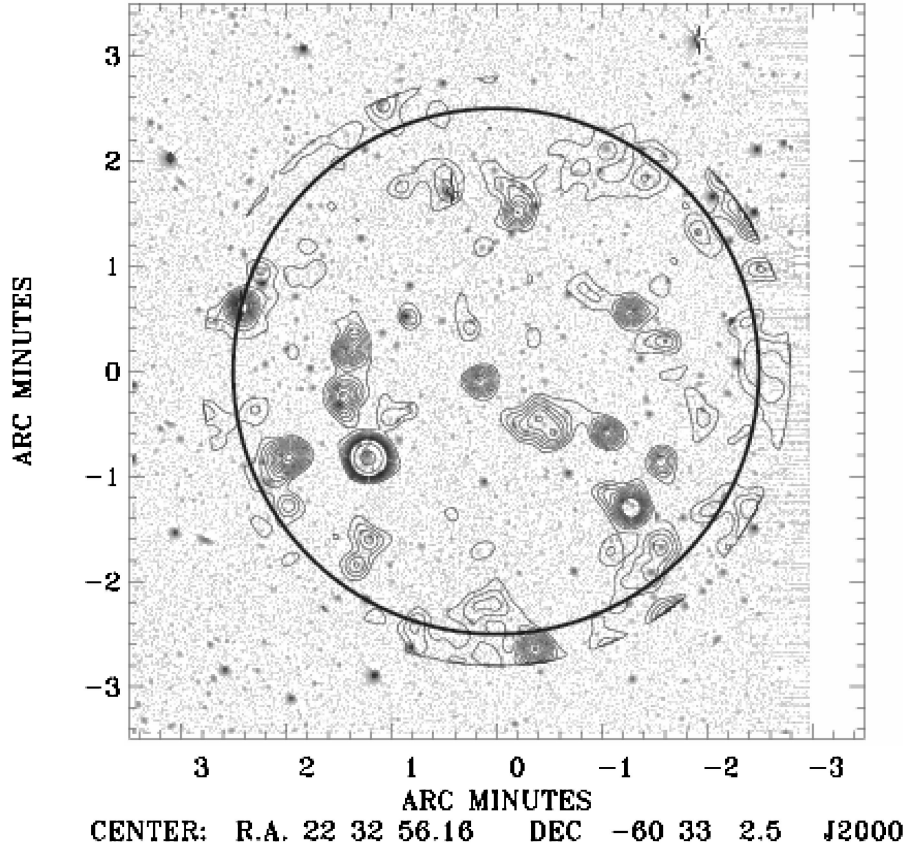


**Figure 6.** LW3 (15  $\mu\text{m}$ ) signal-to-noise ratio map. This Fig. plots contours in the LW3 signal-to-noise ratio map after it has been smoothed with the point-source-detection kernel. The lowest contour level has signal-to-noise ratio = 1 and subsequent intervals are 1 until signal-to-noise ratio = 10 after which the contours are logarithmically spaced. *ISO* data are plotted out to a radius of 2.8 arcmin. The background image is the CTIO BTC survey of Walker (1999). The circle indicates the 2.5-arcmin boundary of the region within which we extracted sources for our catalogues. Overlays of subsections of the data on to colour *HST* images are available from our WWW page (<http://astro.ic.ac.uk/hdfs>).

**Table 4.** Full width to half-maxima (FWHM, in arcsec) for theoretical and empirical PSFs: see text for details. The column marked ‘Used’ gives the FWHM values for the model PSFs used for source extraction; the ‘Star’ PSF is estimated from the brightest star in the LW2 image, and the ‘Sources’ PSF from the sources detected above  $20\sigma$  in each image (eight sources for LW2 and one source for LW3). Empirical FWHM are calculated by fitting a 2D Gaussian to the observed PSF.

Filter	$\lambda(\mu\text{m})$	Airy disc + pixel	CIA	Used	Star	Sources
LW2	6.7	5.8	7.3	6.0	10.4	8.3
LW3	15	7.3	9.0	10.0		10.4

practice, however, the PSF will be broadened by our mapping footprint, and any inaccuracies in registration and/or the field-distortion correction applied. The profiles that we use for source extraction are Gaussian, with FWHM of 6 and 10 arcsec at 6.7 and 15  $\mu\text{m}$  respectively, and both are truncated at a radius of 12 arcsec. Table 4 compares the FWHM values for these model PSFs with those estimated from the sources detected in the data. It shows that, as desired, the model PSFs used for source detection, while being slightly larger than the theoretical PSF, are slightly narrower than the empirical PSF derived from the sources themselves.

An initial candidate list of sources is selected in each band, comprising peaks in the respective convolved, co-added signal-to-noise ratio (*SNRO*) map above  $3\sigma$ . For each of these peaks we

return to the individual raster maps and compute a number of additional statistics. These include the signal-to-noise ratio in each map ( $SNR_n, n = 1-4$ ) and the number of pointings at the source position in these maps ( $NPOINT_n, n = 1-4$ ). One quantity derived ( $PICK$ ) is the number of detections with  $SNR_n > 1$  and  $NPOINT_n > 4$ . We also compute the mean and rms deviation of the flux for the source over all maps, together with the ratio of these ( $SNR5$ ). Using the simulations described in Section 6 we can then assess and employ these various statistics to define suitable simple criteria for filtering the candidate list to produce a highly reliable source list with reasonable completeness.

## 5 PHOTOMETRIC CALIBRATION

One difference between the HDF-S and the HDF-N is that the former is located at lower Galactic latitude and so has a higher proportion of stars. This is extremely useful for the calibration of the *ISO* data, since a number of the bright stars are detected, and photospheric model spectra can be used to estimate their 6.7- and 15- $\mu\text{m}$  fluxes. Our calibration procedure is to identify a number of stars for which we can accurately predict mid-infrared fluxes and then measure their fluxes directly from the *ISO* maps. Since the stars are known sources with known positions we are not concerned about the reliability of their detection, so these stars do not necessarily appear in our source lists, and their fluxes can be fainter than the faintest sources in our complete samples.

**Table 5.** Stars in HDF-S. This is an inhomogeneous list of stars collected for the process of calibration. Spectral types were determined from the AAT spectra. Optical magnitudes are in the AB system and come from the ESO survey (da Costa et al. 1998) or the AAT survey (Verma et al., in preparation). Observed 6.7- and 15- $\mu\text{m}$  fluxes ( $S_o$ ) are in raw instrumental units. Fluxes are taken directly from the maps. One flux was measured to be negative (with large error) and is quoted as such, since this would be valid in a calibration fit; however, this point has not been used in the calibration. Predicted 6.7- and 15- $\mu\text{m}$  fluxes ( $S_p/\mu\text{Jy}$ ) are estimated for a few of these objects as described in the text. Magnitudes quoted as 99.99 indicate saturated measurements.

RA, Dec. (J2000)	Type	<i>U</i>	<i>B</i>	<i>V</i>	<i>R</i>	<i>I</i>	<i>J</i>	<i>H</i>	<i>K</i>	$S_{o6.7}$	$S_{o15}$	$S_{p6.7}$	$S_{p15}$
22 32 31.94 – 60 32 00.7			11.94		12.17					77.42	23.79		
22 32 36.19 – 60 34 31.5		21.56	19.81	18.14	17.00	15.80				17.66	10.79	626.0	134.0
22 32 36.23 – 60 31 31.5		20.38	18.51	16.92	15.80	14.60				42.17	26.01	600.0	130.0
22 32 37.48 – 60 32 57.3		21.30	19.38	17.73	16.70	15.70				12.56	6.33	611.0	134.0
22 32 39.41 – 60 31 22.6	G0 V	18.02	17.03	16.38	16.10	16.00				2.17	7.23		
22 32 39.88 – 60 33 23.6	M2.5 V	99.99	99.99	99.99	99.99	26.40				0.40	5.38		
22 32 40.70 – 60 33 24.1										0.39	5.30		
22 32 43.51 – 60 33 51.0		20.51	20.11	20.23	20.01	19.85	19.78	19.42	19.53	4.35	10.76		
22 32 47.45 – 60 32 00.0	M2.5 V	99.99	24.05	22.59	21.31	19.80	18.36	18.22	18.42	0.45	– 1.17		
22 32 50.50 – 60 34 00.8	M2 V	21.98	20.24	18.71	17.90	17.13	16.41	16.21	16.49	3.74	0.96		
22 32 50.62 – 60 34 04.0		21.90	20.23	18.70	17.84	17.01	16.42	16.21	16.49	3.74	1.30	166.0	36.5
22 32 54.90 – 60 31 44.1		23.41	21.70	20.18	19.30	18.32	17.51	17.26	17.51	0.92	6.34		
22 32 56.72 – 60 35 49.5		27.63	25.81	24.35	23.50	22.90				1.00	9.69		
22 32 59.50 – 60 31 19.2	G2 III	15.11	14.63	13.91	14.14	13.60	13.57	13.61	14.03	20.82	6.43	1096.0	230.0
22 33 02.70 – 60 35 39.5		20.79	18.98	17.77	17.22	16.80	16.67	16.51	16.86	2.33	7.42		
22 33 02.76 – 60 32 13.3	M3 V	23.00	21.26	19.76	18.87	17.74	16.90	16.76	17.01	1.38	0.70	105.0	23.0
22 33 03.07 – 60 32 30.8	M1 V	20.01	18.15	16.83	16.20	15.53	14.97	14.73	15.04	9.29	4.28	550.0	118.0
22 33 08.20 – 60 33 21.2	K4 V				17.30		16.75	16.57	16.97	1.91	12.14		
22 33 12.09 – 60 34 16.7							22.46	21.76	21.10	1.39	8.16		
22 33 15.83 – 60 32 24.0	M2 V		15.80		13.95	13.11	12.47	12.24	12.53	90.78	31.03	6000.0	1311.0
22 33 19.00 – 60 32 27.8	M2 V				20.83					1.53	6.40		
22 33 20.83 – 60 34 35.1	G1 V				17.10						6.74		
22 33 24.02 – 60 33 10.6	G3.5 V				17.91					0.78			
22 33 24.22 – 60 33 52.9	M3 V				16.32					16.07	15.89		
22 33 26.22 – 60 32 05.9	F8 III				15.93								
22 33 28.05 – 60 33 38.0	G5 V				19.96								
22 33 28.93 – 60 35 01.5	M2.5 V				21.53								
22 33 31.23 – 60 33 43.9	M3 V				19.48								
22 33 31.67 – 60 33 41.9	M2 V				24.04								
22 33 37.40 – 60 34 03.2	M3 V				18.84								
22 33 46.17 – 60 34 03.4	M2 III				19.95								

To model the stellar fluxes accurately we ideally need spectral classifications and accurate magnitudes for the stars. We inspect and classify the star spectra taken on the Anglo-Australian Telescope (AAT) with the Low Dispersion Survey Spectrograph (LDSS) (Glazebrook et al., in preparation; see <http://www.aao.gov.au/hdfs/Redshifts/>). We supplement this list with additional stars that have been detected in our *ISO* maps (prior to the filtering applied to produce a highly reliable source list presented in Section 7). We cross-correlate all these objects with the European Southern Observatory (ESO) optical catalogues (da Costa et al. 1998) and the AAT catalogues (Verma et al., in preparation) to obtain optical and near-infrared magnitudes. This combined sample of stars is listed in Table 5.

For each star we return to the *ISO* maps and extract the flux and uncertainty in the flux, exactly as we did for our *ISO*-detected source list. For a number of them that had good *ISO* detections at 6.7  $\mu\text{m}$  and good optical information, we estimate the expected 6.7- and 15- $\mu\text{m}$  fluxes using the models of Kurucz.<sup>4</sup> Where a spectral classification is not available, the temperature is estimated from the optical photometry alone. The predicted fluxes are plotted against the observed fluxes for the two wavebands in Figs 7 and 8. We have performed a linear fit to these data constrained to pass through the origin. For the 6.7- $\mu\text{m}$  data we exclude the star at 22<sup>h</sup> 32<sup>m</sup> 36<sup>s</sup>23, –60°31′31″5, which is a significant outlier and has neither a spectral type nor near-infrared magnitudes. For the

15- $\mu\text{m}$  data we exclude 22<sup>h</sup> 32<sup>m</sup> 36<sup>s</sup>23, –60°31′31″5, as we had at 6.7  $\mu\text{m}$ , and also 22<sup>h</sup> 32<sup>m</sup> 36<sup>s</sup>19, –60°34′31″5, which is an outlier in both fits and also has neither near-infrared nor classification information. The fits are remarkably good once the few outliers have been excluded, and provide us with a good flux calibration, which is used throughout this paper. From the scatter in the correlation the errors in this calibration are estimated to be 36 per cent at 6.7  $\mu\text{m}$  and 28 per cent at 15  $\mu\text{m}$ .

## 6 SIMULATIONS

The noise properties of the *ISO* data are sufficiently complicated that simulations are essential in order to determine accurately the quality of the information extracted from our maps. In particular we wish to assess the reliability of the source catalogues presented in Section 7 and to calculate the effective area over which we could have detected sources above a given flux limit, to facilitate computation of source counts in Section 8. We have thus constructed a number of simulated data sets which mimic the noise properties of the real data as faithfully as possible.

### 6.1 Method

As discussed earlier, most sources will not be detected significantly in individual time-lines, only appearing after co-addition of many observations of the same patch of sky. By corrupting the astrometric information before constructing the maps it is thus possible to remove most of the real source signal, the remaining

<sup>4</sup> See <http://kurucz.harvard.edu/>

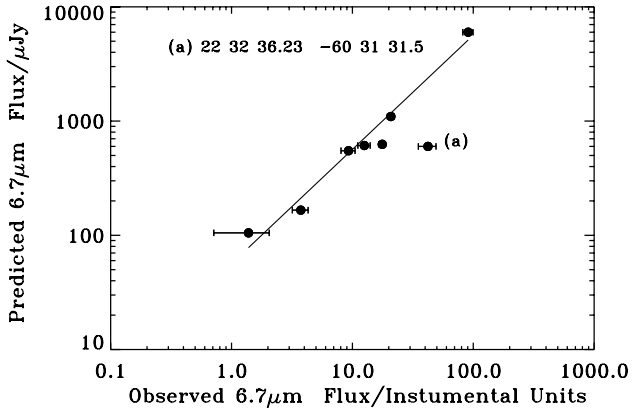


**Figure 7.** Calibration of the 6.7- $\mu\text{m}$  data. The linear fit is constrained to pass through the origin and excludes source  $22^{\text{h}}32^{\text{m}}36^{\text{s}}.23$ ,  $-60^{\circ}31'31''.5$ . The fit is  $S_p/\mu\text{Jy} = 56 \pm 20S_o/\text{Instrumental Unit}$ .

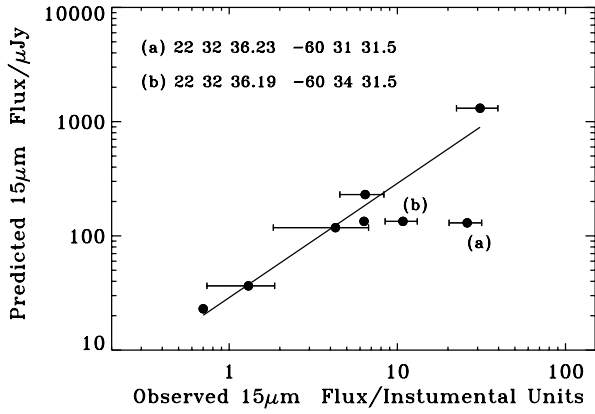


**Figure 8.** Calibration of the 15- $\mu\text{m}$  data. The linear fit is constrained to pass through the origin and excludes sources  $22^{\text{h}}32^{\text{m}}36^{\text{s}}.23$ ,  $-60^{\circ}31'31''.5$  and  $22^{\text{h}}32^{\text{m}}36^{\text{s}}.19$ ,  $-60^{\circ}34'31''.5$ . The fit is  $S_p/\mu\text{Jy} = 29 \pm 8S_o/\text{Instrumental Unit}$ .

fluctuations being almost entirely due to noise. This technique was employed in our reduction of the HDF-N data, where we corrupted the astrometric information by randomizing the apparent location of each pixel within the detector array for each pointing position. This technique was not entirely satisfactory, since noise that was correlated between neighbouring pointings and pixels was also artificially reduced in the resulting maps. A much better technique is to corrupt the astrometric information coherently for the whole detector, so that real sources are still dispersed, while maintaining the time-ordering of the data, and the localization of pixel groups. This technique should account for all sources of instrumental noise. There are seven possible ways of achieving this for a given raster, corresponding to each independent reflection and rotation of the detector through  $90^\circ$ . Real sources that happen to lie near the axis of symmetry in some pointings will be less corrupted than others, so we expect the resulting ‘noise’ maps to have some fluctuations caused by real sources and they are thus pessimistic estimates of the noise. For each observation we generate all seven possible ‘noise’ maps. Since the HDF-S field is observed four times with each band, there are thus  $7^4 = 2401$  different combinations of ‘noise’ maps that we can use to simulate a completed map.

One source of noise that is not included in these ‘noise’ maps is

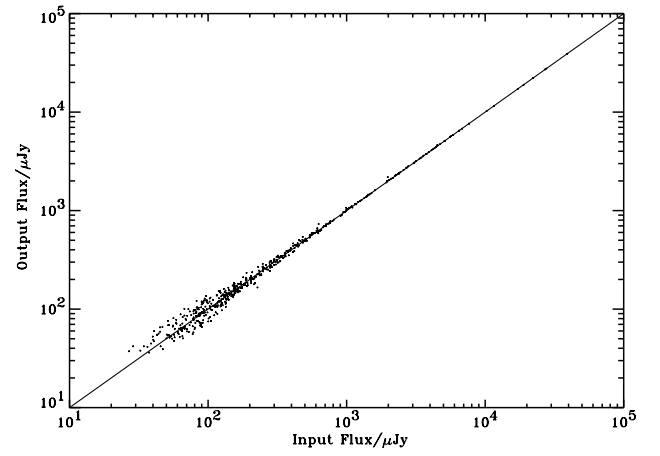


**Figure 9.** Output flux vs. Input flux from the simulated data at 6.7  $\mu\text{m}$ .

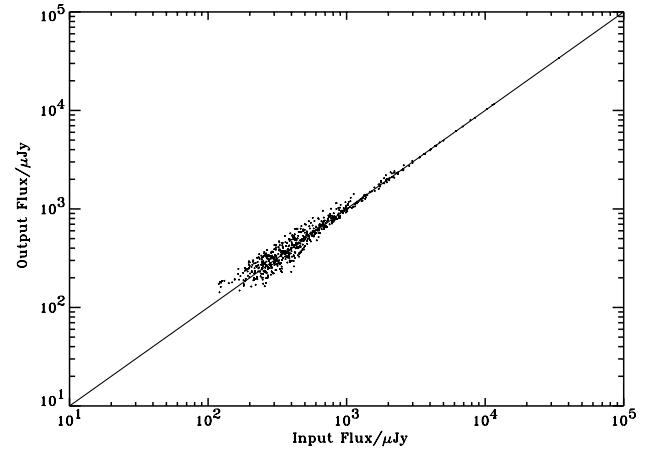


**Figure 10.** Output flux vs. Input flux from the simulated data at 15  $\mu\text{m}$ .

confusion noise arising from real sources. To account for this we generate artificial source lists generated from a number count distribution which is a reasonable fit to a preliminary analysis of the total source counts (i.e. including both stars and galaxies). We generate 25 independent synthetic source lists and add each of these source lists to a randomly selected set of ‘noise’ maps, using the empirical PSF discussed in Section 4. The sources are placed on the maps at their nominal positions, and thus we do not include any additional uncertainties in the field distortions or registration, which will be taken into account by our use of an empirical PSF. The resulting maps are co-added and processed to produce source lists in exactly the same fashion as the real data.

## 6.2 Results

Having extracted the sources from the simulated maps, we can immediately use these to check for any biases or non-linearities in our flux estimation, either from the peculiarities in the data reduction process or from the properties of the sky itself. Biases from the sky might arise through confusion (where faint sources are blurred together and add flux to identified sources) or Eddington bias (sometimes called Malmquist bias, where, even with a symmetric noise distribution, if the source counts are rising more sources are randomly scattered to brighter fluxes than are randomly scattered to fainter fluxes). The first step is to associate

the detected sources with the corresponding input source. To do this we use a 4-arcsec search radius and require that the ratio of the output and input fluxes does not exceed  $\pm 0.3$  dex.

The resulting comparisons are shown in Figs 9 and 10. At 6.7  $\mu\text{m}$  the results are highly linear and there appears to be no significant bias, while at 15  $\mu\text{m}$ , where we expect the confusion noise to be higher, there is some evidence for a small tendency to over-estimate faint fluxes. For the purposes of this paper we ignore these small flux biases.

## 7 CATALOGUES

The simulations of Section 6 have been used to investigate how to construct a highly reliable source list that can be described simply in terms of the quantities introduced in Section 4. We eventually decided on the following criteria:

- (i)  $SNR0 > 3$ : the initial candidate selection from the co-added maps;
- (ii) all candidates located within a 2.5-arcmin radius of  $22^{\text{h}} 32^{\text{m}} 56^{\text{s}}.2$ ,  $-60^{\circ} 33' 27.7$  (J2000): this excludes regions of low *NPOINT*, non-Gaussian and/or higher noise, giving a clean and simple selection criterion;
- (iii)  $SNR5 > 1$ : this excludes spurious sources generated from a strong noise feature in one map;
- (iv) for LW2 only,  $PICK > 3$ .

These criteria result in 24 sources being detected in the LW2 maps and an equal number being detected in the LW3 maps: from the simulations we estimate that the resulting source lists have 2.3 and 2.4 spurious sources, respectively, implying a reliability of about 90 per cent. The ‘completeness’ of these lists, expressed as an effective survey area, is discussed in Section 8.

For ease of comparison of our results with those from any

possible future reductions of these data by other methods, we present our source catalogues with fluxes given in both instrumental and physical units, thereby decoupling issues of source detection, reliability and completeness from that of photometric calibration. In Tables 6 and 7 we list the separate source catalogues for the two bands, while Table 8 presents the results of merging these two catalogues. This is done by associating sources from different bands separated by less than 5 arcsec, which produces 13 matches. The 5-arcsec radius is chosen to be slightly less than the Airy radius at 15  $\mu\text{m}$  (6 arcsec), larger than the astrometric errors which are discussed further in Paper II, yet small enough that there is little danger of association with an unrelated neighbouring source (the number of unrelated sources expected in a circle this size is 0.03, assuming a Poisson distribution). For those sources where no such match is found, we return to the smoothed signal-to-noise ratio map and, if we find a signal-to-noise ratio above 2, we use the peak flux at this position (the assumption being that the rejection criteria which are applied to ensure reliability are not necessary since we have a confirmed detection in the other wavelength). Otherwise we determine an upper limit, being the flux that would have given the observed smoothed signal if the noise fluctuation were  $-2\sigma$ . The absolute reference frame of the *ISO* data is set by making the position of the brightest 15- $\mu\text{m}$  source, ISOHDFSC15 J223306-603350, coincident with that of the bright radio source HDFS J223306.0-603350 (A. Hopkins, private communication) with which it is clearly associated, and then optimizing the match between the *ISO* and optical positions of several of the bright stellar identifications of Paper II: this latter procedure only shifts the astrometric frames of the 6.7- and 15- $\mu\text{m}$  data by  $\sim 1$  arcsec each.

The resulting  $S_{6.7}/S_{15}$  colour–flux diagram is shown in Fig. 11. Notice a reasonably clear distinction between stars and galaxies. For  $\log_{10}(S_{6.7}/S_{15}) > 0.1$  all sources with an identification are morphologically classified as stars and occupy, or are consistent

**Table 6.** Sources selected at 7  $\mu\text{m}$ . Signal-to-noise ratio is estimated from the smoothed, co-added map. Flux ( $S$ , in instrumental units) is estimated from the peak in the smoothed map; the error is estimated from the standard deviation of the peak flux from independent rasters.  $SNR5$  is  $S/\sigma$ .  $PICK$  is the number of independent  $SNRn > 1$  detections.

Name	RA & Dec. (J2000)	SNR	$S$	$\sigma$	$SNR5$	$PICK$
ISOHDFSC7 J223315-603224	22 33 15.75 – 60 32 24.0	205.8	5083.7	492.8	10.0	4
ISOHDFSC7 J223259-603118	22 32 59.50 – 60 31 18.9	66.6	1165.9	74.6	15.8	4
ISOHDFSC7 J223306-603349	22 33 06.08 – 60 33 49.1	62.2	943.0	8.3	113.9	4
ISOHDFSC7 J223303-603230	22 33 03.04 – 60 32 30.6	38.8	520.2	69.1	7.6	4
ISOHDFSC7 J223237-603256	22 32 37.50 – 60 32 56.7	32.3	699.4	79.4	8.6	4
ISOHDFSC7 J223243-603351	22 32 43.63 – 60 33 51.0	15.1	242.5	30.2	8.1	4
ISOHDFSC7 J223250-603359	22 32 50.58 – 60 33 59.9	14.9	209.4	31.4	6.7	4
ISOHDFSC7 J223243-603242	22 32 43.03 – 60 32 42.2	10.6	171.9	39.9	4.1	4
ISOHDFSC7 J223312-603350	22 33 12.36 – 60 33 50.7	10.6	209.4	68.4	3.2	4
ISOHDFSC7 J223243-603441	22 32 43.57 – 60 34 41.6	9.1	193.2	42.0	4.6	4
ISOHDFSC7 J223245-603418	22 32 45.53 – 60 34 18.0	8.3	140.6	56.7	2.5	4
ISOHDFSC7 J223308-603317	22 33 08.13 – 60 33 17.8	6.8	107.0	25.6	4.0	4
ISOHDFSC7 J223237-603235	22 32 37.99 – 60 32 35.5	5.9	122.1	46.3	2.4	4
ISOHDFSC7 J223303-603336	22 33 03.43 – 60 33 36.0	5.5	76.2	14.1	5.1	4
ISOHDFSC7 J223302-603213	22 33 02.62 – 60 32 13.3	5.3	77.3	37.6	2.2	4
ISOHDFSC7 J223256-603059	22 32 56.79 – 60 30 59.2	4.9	98.0	35.2	2.7	4
ISOHDFSC7 J223247-603336	22 32 47.81 – 60 33 36.6	4.5	63.8	41.0	1.6	4
ISOHDFSC7 J223302-603323	22 33 02.76 – 60 33 23.5	4.5	62.2	12.5	4.9	4
ISOHDFSC7 J223253-603328	22 32 53.07 – 60 33 28.1	4.3	56.0	20.1	2.7	3
ISOHDFSC7 J223254-603115	22 32 54.95 – 60 31 15.1	3.4	62.2	28.4	2.3	3
ISOHDFSC7 J223254-603127	22 32 54.55 – 60 31 27.8	3.0	51.0	19.3	2.5	3
ISOHDFSC7 J223302-603137	22 33 02.12 – 60 31 37.5	4.3	70.6	46.2	1.4	3
ISOHDFSC7 J223307-603247	22 33 07.53 – 60 32 47.0	4.1	64.4	30.0	2.0	3
ISOHDFSC7 J223254-603143	22 32 54.92 – 60 31 43.8	3.5	51.5	23.2	1.8	3

**Table 7.** Sources selected at 15  $\mu\text{m}$ . Signal-to-noise ratio is estimated from the smoothed, co-added map. Flux ( $S$ , in instrumental units) is estimated from the peak in the smoothed map; the error is estimated from the standard deviation of the peak flux from independent rasters.  $SNR5$  is  $S/\sigma$ .  $PICK$  is the number of independent  $SNRn > 1$  detections.

Name	RA & Dec. (J2000)	SNR	$S$	$\sigma$	$SNR5$	$PICK$
ISOHDFSC15 J223306-603350	22 33 06.08 – 60 33 50.0	50.8	2274.2	15.8	142.1	4
ISOHDFSC15 J223245-603418	22 32 45.72 – 60 34 18.3	15.4	826.5	70.8	11.7	4
ISOHDFSC15 J223315-603223	22 33 15.81 – 60 32 23.6	12.4	899.9	248.4	3.3	4
ISOHDFSC15 J223312-603349	22 33 12.25 – 60 33 49.6	10.5	617.1	67.6	8.6	4
ISOHDFSC15 J223247-603335	22 32 47.63 – 60 33 35.5	8.7	385.1	156.1	2.3	4
ISOHDFSC15 J223307-603248	22 33 07.54 – 60 32 48.8	8.6	399.6	66.8	5.2	4
ISOHDFSC15 J223245-603226	22 32 45.81 – 60 32 26.1	8.4	412.7	56.7	6.7	4
ISOHDFSC15 J223257-603305	22 32 57.42 – 60 33 05.7	8.1	308.8	118.0	2.4	4
ISOHDFSC15 J223308-603314	22 33 08.01 – 60 33 14.9	7.6	352.1	96.4	3.5	4
ISOHDFSC15 J223254-603129	22 32 54.49 – 60 31 29.7	7.1	361.6	96.5	3.3	4
ISOHDFSC15 J223251-603335	22 32 51.81 – 60 33 35.1	6.2	255.2	56.1	4.2	4
ISOHDFSC15 J223252-603327	22 32 52.87 – 60 33 27.9	6.1	239.8	58.2	3.7	4
ISOHDFSC15 J223243-603351	22 32 43.42 – 60 33 51.6	5.9	310.9	4.4	70.6	3
ISOHDFSC15 J223243-603440	22 32 43.44 – 60 34 40.7	4.7	312.0	158.9	2.0	4
ISOHDFSC15 J223306-603436	22 33 06.05 – 60 34 36.6	4.3	241.6	95.6	2.8	3
ISOHDFSC15 J223306-603450	22 33 06.99 – 60 34 50.8	4.2	242.4	64.0	3.8	3
ISOHDFSC15 J223243-603243	22 32 43.12 – 60 32 43.3	4.1	216.9	88.6	2.5	3
ISOHDFSC15 J223312-603416	22 33 12.25 – 60 34 16.9	3.7	236.6	72.2	3.1	3
ISOHDFSC15 J223244-603455	22 32 44.22 – 60 34 55.3	3.5	239.5	99.0	2.6	3
ISOHDFSC15 J223256-603513	22 32 56.46 – 60 35 13.2	3.4	217.8	31.8	6.8	3
ISOHDFSC15 J223259-603116	22 32 59.90 – 60 31 16.6	3.3	185.3	48.6	3.6	4
ISOHDFSC15 J223244-603110	22 32 44.70 – 60 31 10.0	3.1	242.7	52.9	4.7	3
ISOHDFSC15 J223240-603141	22 32 40.53 – 60 31 41.0	3.1	235.5	45.6	5.3	4
ISOHDFSC15 J223314-603203	22 33 14.40 – 60 32 03.4	3.3	240.1	178.2	1.0	2

with, a well-defined stellar locus with  $\log_{10}(S_{6.7}/S_{15}) \sim 0.7$ . Below  $\log_{10}(S_{6.7}/S_{15}) < -0.3$  everything is morphologically non-stellar. In between these two limits are a mixture of sources. First, there are three stars that have upper limits at 15  $\mu\text{m}$  within this part of the diagram but are consistent with the colours of the other stars. Secondly, there is one source (ISOHDFS J223243-603351) which has a broad line in its optical spectrum, and we thus assume that the relatively warm *ISO* colours are because the infrared emission arises from a dusty torus being heated by an active galactic nucleus (AGN). This region and above also contains two of the three objects that have no reliable optical association (ISOHDFS J223256-603059 and J223302-603137) as discussed in Paper II, and a third (ISOHDFS J223314-603203) which is one of the most uncertain identifications made there: in that paper we note that each of these is located close to a bright star, which may mean that the sources are spurious and will certainly affect their *ISO* colours. Of the four galaxies located firmly within this region, we show in Paper II that three have spectral energy distributions (SEDs) consistent with normal spiral or cirrus galaxies (ISOHDFS J223243-603441, J223302-603323 and J223303-603336; the last of these has only an upper limit at 15  $\mu\text{m}$ ), while the fourth, ISOHDFS J223243-603242, does appear to have anomalously low 15- $\mu\text{m}$  flux indicating perhaps a deeper rest-frame 10- $\mu\text{m}$  absorption. Finally, two galaxies lie on the lower colour limit: one of these (ISOHDFS J223306-603349) is a bright spiral galaxy with a normal spiral SED, while the second (ISOHDFS J223254-603115) is associated with one of a pair of possibly interacting galaxies: this confuses the optical magnitudes and is also likely to confuse the *ISO* colours. We also note that ISOHDFS J223256-603513, for which we are unable to make a secure optical identification, was the only source for which we recorded a negative 6.7- $\mu\text{m}$  flux measurement when determining the upper limits.

In conclusion, it appears that the 6.7- $\mu\text{m}$ /15- $\mu\text{m}$  flux ratio separates quite neatly stars from star-forming galaxies, with AGN

and normal galaxies occupying a middle ground. The *ISO* colours appear consistent with our optical morphological classifications: for the purposes of this paper we will use the morphological classifications and for the number count analysis we will exclude the unidentified sources.

## 8 SOURCE COUNTS

### 8.1 Calculation of effective area

From the simulated catalogues we can directly determine the ‘completeness’, which we define in terms of the effective area as a function of flux, the effective area of the catalogue, at a given flux, being the area within which a source of that flux could have been detected. We can estimate this from the simulations by determining the fraction of sources of a given input flux that pass all our selection criteria, and the effective area is then this fraction of the area over which the input catalogues were prepared; in practice we examine only those input sources that fall within a 2.5-arcmin radius of  $22^{\text{h}}32^{\text{m}}56^{\text{s}}.2, -60^{\circ}33'27''$  (J2000). If the output flux is an unbiased estimator of the input flux, this estimate of the effective area is unbiased. Eddington bias and confusion noise do cause some bias, as discussed in Section 6, but these appear to be small and are only second-order effects in the calculation of effective area so we ignore them here. The resulting effective areas are illustrated in Figs 12 and 13.

As with the ELAIS 6.7- and 15- $\mu\text{m}$  counts (Serjeant et al. 2000), we fit the histogram of the effective area with a hyperbolic tan function  $\Omega = 19.63 \frac{1}{2} \tanh[a \log_{10}(S/b) + 1]$ , where  $a$  defines the gradient of the decline and  $b$  defines its location. For the 6.7- $\mu\text{m}$  simulations we find  $a = 4.47$  and  $b = 61.1 \mu\text{Jy}$ , while for the 15- $\mu\text{m}$  simulations we find  $a = 3.70$  and  $b = 275 \mu\text{Jy}$ . Also illustrated in Figs 12 and 13 are estimates of the effective area naively based on the noise maps used in constructing the signal-to-noise

**Table 8.** Merged *ISO* HDF-S source list. The 6.7- and 15- $\mu\text{m}$  sources have been cross-correlated using a 5-arcsec search radius, and fluxes for non-matches are determined from the maps. Upper limits are also estimated from the maps and denoted by ‘ $<S_{\text{up}}$ ’, where  $S_{\text{up}} = S_{\text{obs}} + 2\sigma$ ;  $\sigma$  is estimated from the scatter between independent maps at the source position and  $S_{\text{obs}}$  is the recorded flux at the source position (which may be negative). Sources marked with an asterisk do not have optical identifications (see Paper II). In most cases they are located near another bright source and are very likely to be spurious: their number is consistent with our simulations, and these ‘sources’ have not been used in our number count analysis.

Name	$S_{6.7}$ / $\mu\text{Jy}$	$\sigma_{6.7}$ / $\mu\text{Jy}$	$S_{15}$ / $\mu\text{Jy}$	$\sigma_{15}$ / $\mu\text{Jy}$
ISOHDFS J223237-603256	699.4	79.4	< 389.9	168.4
ISOHDFS J223237-603235	122.1	46.3	< 321.1	122.5
ISOHDFS J223240-603141	< 119.4	43.7	235.5	45.6
ISOHDFS J223243-603242	171.9	39.9	216.9	88.6
ISOHDFS J223243-603441	193.2	42.0	312.0	158.9
ISOHDFS J223243-603351	242.5	30.2	310.9	4.4
ISOHDFS J223244-603455	< 53.6	21.3	239.5	99.0
ISOHDFS J223244-603110	< 90.4	31.4	242.7	52.9
ISOHDFS J223245-603418	140.6	56.7	826.5	70.8
ISOHDFS J223245-603226	< 46.7	19.3	412.7	56.7
ISOHDFS J223247-603335	63.8	41.0	385.1	156.1
ISOHDFS J223250-603359	209.4	31.4	< 101.9	66.5
ISOHDFS J223251-603335	31.6	28.9	255.2	56.1
ISOHDFS J223252-603327	56.0	20.1	239.8	58.2
ISOHDFS J223254-603129	51.0	19.3	361.6	96.5
ISOHDFS J223254-603143	51.5	23.2	< 53.9	20.2
ISOHDFS J223254-603115	62.2	28.4	152.5	57.2
ISOHDFS J223256-603513*	< 43.7	30.1	217.8	31.8
ISOHDFS J223256-603059*	98.0	35.2	< 134.8	59.1
ISOHDFS J223257-603305	< 69.3	22.6	308.8	118.0
ISOHDFS J223259-603118	1165.9	74.6	185.3	48.6
ISOHDFS J223302-603137*	70.6	46.2	< 12.1	9.0
ISOHDFS J223302-603213	77.3	37.6	< 143.3	70.8
ISOHDFS J223302-603323	62.2	12.5	82.5	106.0
ISOHDFS J223303-603230	520.2	69.1	114.9	65.1
ISOHDFS J223303-603336	76.2	14.1	< 74.7	40.6
ISOHDFS J223306-603436	49.8	19.8	241.6	95.6
ISOHDFS J223306-603349	943.0	8.3	2274.2	15.8
ISOHDFS J223306-603450	< 87.4	41.3	242.4	64.0
ISOHDFS J223307-603248	64.4	30.0	399.6	66.8
ISOHDFS J223308-603314	107.0	25.6	352.1	96.4
ISOHDFS J223312-603416	61.2	65.0	236.6	72.2
ISOHDFS J223312-603350	209.4	68.4	617.1	67.6
ISOHDFS J223314-603203	100.5	82.8	240.1	178.2
ISOHDFS J223315-603224	5083.7	492.8	899.9	248.4

ratio maps. Since this ignores some of the selection criteria, it overpredicts the fraction of sources detectable at brighter fluxes. On the other hand, it takes no account of the boosting of faint input fluxes by confusion noise or Eddington bias, and so underpredicts the effective area at faint fluxes. This illustrates that these simulations at least account for these biases to first order.

## 8.2 Source count results

In Figs 14 and 15 we plot the resulting integral counts for galaxies (as defined by the colour criterion defined in Section 7). For comparison we also show the counts obtained by Oliver et al. (1997) for the HDF-N. In Fig. 15 we also show the counts derived by Aussel et al. (1999) from the same HDF-N data.

At 6.7  $\mu\text{m}$  the galaxy counts from HDF-N and HDF-S are in good agreement at the faint end, but the HDF-S counts are higher at the brighter end. One possible explanation for this is that the original selection of the HDF-N field, which avoided bright galaxies, biased the bright counts downwards. Owing to the observational strategies discussed in Section 2, the HDF-S data at

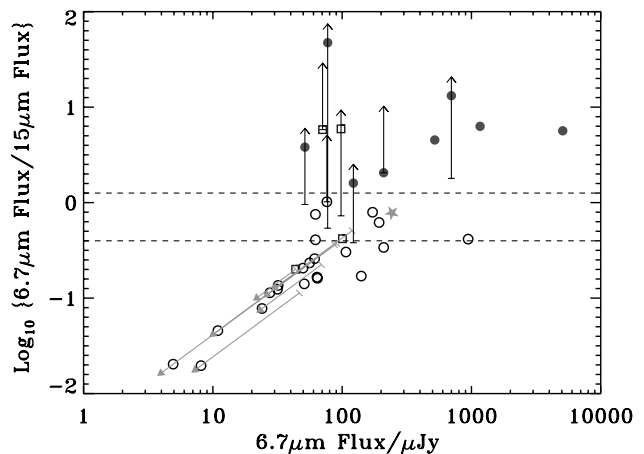


**Figure 11.** 6.7- $\mu\text{m}$ /15- $\mu\text{m}$  colour as a function of 6.7- $\mu\text{m}$  flux. Sources morphologically classified as stars are indicated with filled symbols, while other sources have open symbols. ISOHDFS J223243-603351, which has a broad line in the optical spectrum, is indicated by a five-pointed star. Objects with no reliable optical counterpart are indicated by squares. Upper limits are indicated by arrows: the tail of the arrow begins at the position given by the upper limit; if a positive flux measurement was recorded the plotting symbol is placed at the position inferred from this measurement, otherwise the plotting symbol is placed at the tail of the arrow, which is then of arbitrary length. Upward-pointing arrows indicate upper limits in the 15- $\mu\text{m}$  flux; arrows pointing to the bottom left indicate upper limits in the 6.7- $\mu\text{m}$  flux.

6.7  $\mu\text{m}$  are considerably superior to the data from the HDF-N. The larger areal coverage in particular means that the brighter counts are better constrained. So, while Oliver et al. (1997) suggested that the Pearson & Rowan-Robinson (1996) model could be ruled out, as it overpredicted the number of bright sources, we find that the HDF-S data are much more consistent with the Pearson & Rowan-Robinson model; indeed, the Franceschini et al. (1994) model now appears to be ruled out as it does not predict enough brighter 6.7- $\mu\text{m}$  sources. Such a conclusion is also borne out by the ELAIS counts (Serjeant et al. 2000) which are shown for comparison.

The 15- $\mu\text{m}$  HDF-S data over the range 250–400  $\mu\text{Jy}$  are in striking agreement with the Aussel et al. (1999) HDF-N counts (which push the *ISO* data deeper than those of Oliver et al. 1997). If not coincidental, this agreement would suggest that these populations are at moderate to high redshifts. If all the sources had been located at low redshift, the volume sampled within either HDF area ( $\sim 20 \text{ arcmin}^2$ ) would be small and the fluctuations arising from cosmic variance large: e.g. if the sample were limited to  $z < 0.5$ , the fluctuations in this volume would be  $> 100$  per cent (assuming a cubical geometry and the power spectrum of Peacock & Dodds 1994), while even at  $z < 1$  the fluctuations would be around 80 per cent (e.g. Oliver et al. 2000). Below 250  $\mu\text{Jy}$  the HDF-S counts take a sharp upturn. This flux level is also where the effective area drops, and where we are susceptible to errors in its calculation. We demonstrate in Paper II that many of the sources appear to have modest redshifts and so the agreement between the HDF-N and HDF-S brighter data may be coincidental, and the steep upturn could also be an effect of clustering. It would be possible to combine the HDF-N and HDF-S counts to produce a single determination of the counts over the 250–400  $\mu\text{Jy}$  regime, reducing the statistical errors by a factor of  $\sqrt{2}$ . Given the uncertainty in the effective area below 250  $\mu\text{Jy}$ , both the Pearson & Rowan-Robinson (1996) model and the Franceschini et al. (1994)

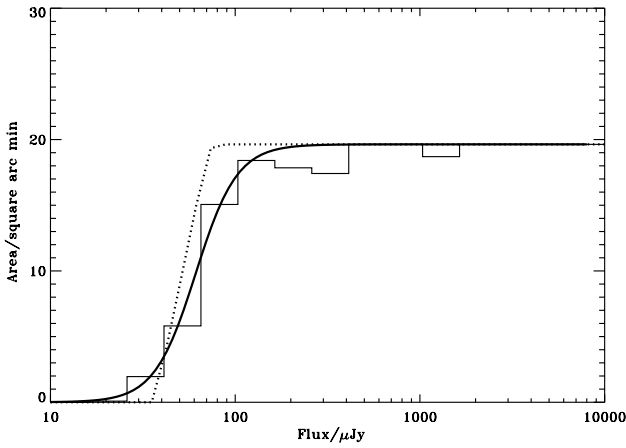


**Figure 12.** 6.7- $\mu\text{m}$  effective area as a function of flux. The histogram is estimated directly from the fraction of sources detected from the simulated data as a function of input source flux. The dotted line is a naive estimate based simply on the signal-to-noise ratio selection criterion and the noise maps, while the solid line is a fit to the simulated histogram:  $\Omega = 19.63 \frac{1}{2} \tanh[4.47 \log_{10}(S/61.1 \mu\text{Jy}) + 1] \text{ arcmin}^2$ .

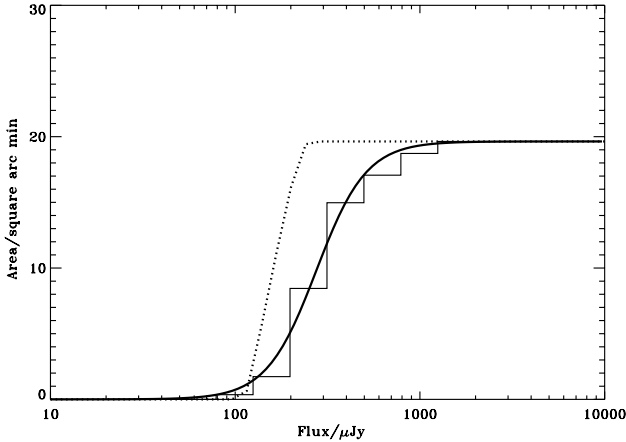


**Figure 13.** 15- $\mu\text{m}$  effective area as a function of flux. The histogram is estimated directly from the fraction of sources detected from the simulated data as a function of input source flux. The dotted line is a naive estimate based simply on the signal-to-noise ratio selection criterion and the noise maps, while the solid line is a fit to the simulated histogram:  $\Omega = 19.63 \frac{1}{2} \tanh[3.70 \log_{10}(S/275 \mu\text{Jy}) + 1] \text{ arcmin}^2$ .

model appear to provide acceptable fits to the counts. Both Guiderdoni et al. (1998) models appear to be too far below the counts.

The star counts at 6.7  $\mu\text{m}$  are shown in Fig. 16. There are currently no published star count data at this wavelength and flux with which to compare these data. However, it is possible to extrapolate from star counts at shorter wavelengths. Minezaki et al. (1998) present near-infrared ( $K$ -band) star counts, towards the South Galactic Pole ( $l = 316^\circ, b = -89^\circ$ ). Converting their differential counts into integral counts and using the  $K$ -band zero-point of 673 Jy, we are able to compare their data with ours. With the exception of their brightest point, their data are fitted with a power law  $\log N(> S) = 4.72 - 0.46 S_K$ . By coincidence, the same power law is consistent with our data. This is consistent with our detecting the same populations, since the slope is the same, but with a higher number density (as we would expect our stars to be fainter). Since we would expect to be in the Rayleigh–Jeans part of a Planck spectrum, we would expect our stars to fainter by a factor

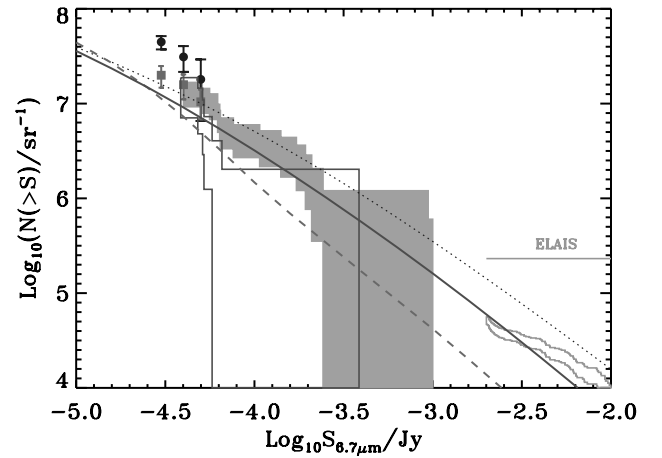


**Figure 14.** Extragalactic counts at 6.7  $\mu\text{m}$  from HDF-S in this work (shaded region). Counts from other surveys are illustrated as follows: Abell 2390 (Altieri et al. 1999, filled circles); Lockman Hole (Taniguchi et al. 1997, filled squares); HDF-N (Oliver et al. 1997, open region at faint fluxes); and ELAIS (Serjeant et al. 2000, open region). The models of Rowan-Robinson (2001) (solid), Pearson & Rowan-Robinson (1996) (dotted) and Franceschini et al. (1994) (short dashed) are plotted for comparison.

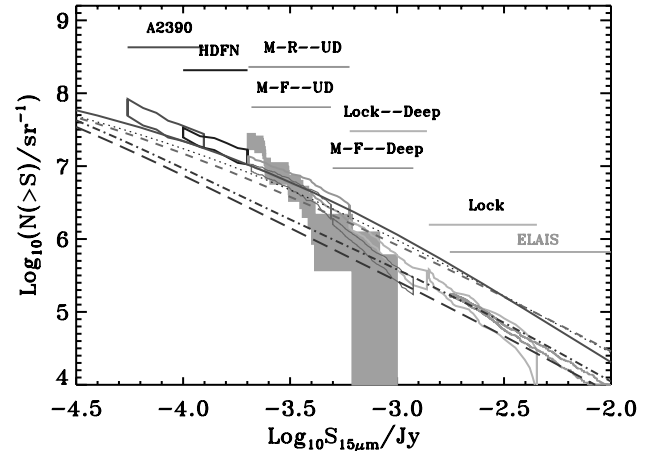


**Figure 15.** Extragalactic source counts at 15- $\mu\text{m}$  with the counts from HDF-S in this work shown as a shaded region. Counts from other surveys are illustrated with open boxes and annotated above, in order of decreasing sensitivity: Abell 2390 (Altieri et al. 1999); Deep HDF-N (Aussel et al. 1999); Marano–*ROSAT* Ultra-deep (Elbaz et al. 1999); Marano–Firback Ultra-deep (thin) (Elbaz et al. 1999); Marano–Firback Deep (thin) (Elbaz et al. 1999); Lockmann Deep (Elbaz et al. 1999); Lockmann Shallow (Elbaz et al. 1999); ELAIS (Serjeant et al. 2000, open region). The models of Rowan-Robinson (2001) (solid), Pearson & Rowan-Robinson (1996) (dotted), Franceschini et al. (1994) (short-dashed), Guiderdoni et al. (1998) model ‘A’ (long-dashed), and Guiderdoni et al. (1998) model ‘E’ (dot-dashed) are plotted for comparison.

of around 11, so the coincidence in normalization thus implies that the HDF-S has about three times the number density of stars as the South Galactic Pole.

## 9 CONCLUSIONS

We have performed a survey using ISOCAM at 6.7 and 15  $\mu\text{m}$  in the *Hubble Deep Field* South region. The observational and data reduction techniques that we have employed mean that these data, and the 6.7- $\mu\text{m}$  data in particular, are significantly improved over the equivalent *ISO* HDF data. From the resulting data we have

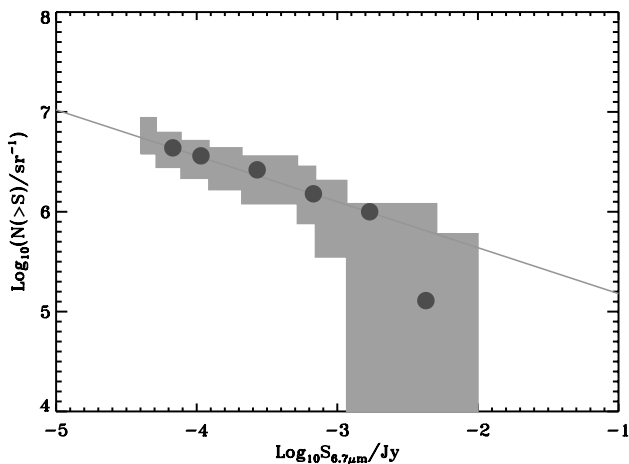


**Figure 16.** The star source counts at 6.7  $\mu\text{m}$  in the HDF-S, shaded region. Circles indicate  $K$ -band star counts in the South Galactic Pole transformed from Minezaki et al. (1998), and the line indicates a fit to those data (excluding the brightest point).

extracted conservative bright source lists. We have thoroughly investigated the completeness and reliability of these lists using simulations. We have performed an external calibration of the data using stars in the field, a number of which have been spectroscopically classified. We find that the 6.7- and 15- $\mu\text{m}$  colour–flux diagram provides a useful discriminant between stars and galaxies. We have investigated the number counts of the extragalactic sources and stars. We find that the number counts of the extragalactic sources are consistent with previous determinations; however, we stress that the volume sampled by our survey is likely to be small and so clustering effects (cosmic variance) may mean that this agreement is somewhat coincidental. A steep upturn at the faintest fluxes is due to only a few sources and is almost certain to be an effect of clustering. Further details of this project can be found at <http://astro.ic.ac.uk/hdfs>.

## ACKNOWLEDGMENTS

We thank the anonymous referee for rapid and constructive feedback. This paper is based on observations with *ISO*, an ESA project, with instruments funded by ESA Member States (especially the PI countries: France, Germany, the Netherlands and the United Kingdom) and with the participation of ISAS and

NASA. This work was in part supported by PPARC grant No. GR/K98728 and EC Network FMRX-CT96-0068. We thank the ATNF HDF-S team, particularly Andrew Hopkins, for providing us with radio data for our sources in advance of publication.

## REFERENCES

- Altieri B. et al., 1999, *A&A*, 343, L65  
 Aussel H., Cesarsky C. J., Elbaz D., Starck J. L., 1999, *A&A*, 342, 313  
 Cesarsky C. J. et al., 1996, *A&A*, 315, L32  
 Cram L., Hopkins A., Mobasher B., Rowan-Robinson M., 1998, *ApJ*, 507, 155  
 da Costa L. et al., 1998, *astro-ph/9812105*  
 Desert F.-X., Puget J.-L., Clements D. L., Perault M., Abergel A., Bernard J.-P., Cesarsky C. J., 1999, *A&A*, 342, 363  
 Elbaz D. et al., 1999, *A&A*, 351, L37  
 Flores H. et al., 1999, *ApJ*, 517, 148  
 Franceschini A., Mazzei P., De Zotti G., Giann F., Danese L., 1994, *ApJ*, 427, 140  
 Gardner J. P. et al., 1999, <http://hires.gsfc.nasa.gov/~gardner/hdfs/>  
 Goldschmidt P. et al., 1997, *MNRAS*, 289, 465  
 Guiderdoni B., Hivon E., Bouchet F. R., Maffei B., 1998, *MNRAS*, 295, 877  
 Kessler M. F. et al., 1996, *A&A*, 315, L27  
 Mann R. G. et al., 1997, *MNRAS*, 289, 482  
 Mann R. G. et al., 2002, *MNRAS*, 332 549 (Paper II, this issue)  
 Minezaki T., Yoshii Y., Cohen M., Kobayashi Y., Peterson B. A., 1998, *AJ*, 115, 229  
 Oliver S. J. et al., 1997, *MNRAS*, 289, 471  
 Oliver S. J. et al., 2000, *MNRAS*, 316, 749  
 Ott S. et al., 1998, in Albrecht R., Hook R. N., Bushouse H. A., eds, *ASP Conf. Ser. Vol. 145, Astronomical Data Analysis Software and Systems VII*. Astron. Soc. Pac., San Francisco, p. 275  
 Peacock J. A., Dodds S. J., 1994, *MNRAS*, 267, 1020  
 Pearson C., Rowan-Robinson M., 1996, *MNRAS*, 283, 174  
 Rowan-Robinson M., 2001, *ApJ*, 549, 745  
 Rowan-Robinson M. et al., 1997, *MNRAS*, 289, 490  
 Serjeant S. B. G. et al., 1997, *MNRAS*, 289, 457  
 Serjeant S. B. G. et al., 2000, *MNRAS*, 316, 768  
 Steidel C. C., Adelberger K. L., Giavalisco M., Dickinson M., Pettini M., 1999, *ApJ*, 519, 1  
 Taniguchi Y. et al., 1997, *A&A*, 328, L9  
 Walker A., 1999, [http://icarus.stsci.edu/~ferguson/hdfstest/hdfs\\_astro.fits](http://icarus.stsci.edu/~ferguson/hdfstest/hdfs_astro.fits)  
 Williams R. E. et al., 1996, *AJ*, 112, 1335

This paper has been typeset from a  $\text{\TeX}/\text{\LaTeX}$  file prepared by the author.